Tailoring zinc diatomic bidirectional catalyst achieving orbital coupling-hybridization for ultralong-cycling zinc-iodine batteries

Chenxu Dong,‡[a] Yongkun Yu,‡[a] Changning Ma,[a] Cheng Zhou,[a] Jiajing Wang,[a] Jiapei Gu,[a] Juan Ji,[a] Shubin Yang,[c] Zunfeng Liu,[d] Xu Xu,*[ab] Liqiang Mai,*[a]

a. State Key Laboratory of Advanced Technology for Materials Synthesis and Processing, International School of Materials Science and Engineering, Wuhan University of Technology, Wuhan 430070, P.R. China

b. Zhongyu Feima New Material Technology Innovation Center (Zhengzhou) Co., Ltd., High Technology Industrial Development Zone, Zhengzhou 450001 P.R. China

c. School of Materials Science and Engineering, Beihang University, 100191, Beijing, China

d. State Key Laboratory of Medicinal Chemical Biology, Key Laboratory of Functional Polymer Materials, College of Chemistry, Nankai University, Tianjin 300071, China

E-mails: xuxu@whut.edu.cn; mlq518@whut.edu.cn

Supporting Information

Experimental Section

In this study, all chemicals were used without further purification. Zinc acetate dihydrate ($C_4H_6O_4Zn·2H_2O$, AR), citric acid monohydrate ($C_6H_8O_7·H_2O$, AR), sodium citrate tribasic dihydrate ($C_6H_5Na_3O_7·2H_2O$, 99%) and dicyandiamide ($C_2H_4N_4$, 98%) were obtained from Aladdin Chemistry Reagent Co. Ltd. Methanol, ethanol were obtained from Aladdin Chemistry Reagent Co. Ltd.

Preparation of carbon substrate.

Trisodium citrate dihydrate (10 g) was dried in an oven at 150°C for 48 hours. Then, lower the reaction temperature to room temperature to obtain white powder and transfer it to a porcelain boat. The white powder was heated at a fixed temperature (800°C) for 1 hour at a rate of 5°C min^{-1} using Ar flow. The harvested black powder was treated with a 5 M H_2SO_4 solution at 80°C for 12 hours, washed multiple times with ultrapure water and ethanol, and dried at 80°C for 6 hours. The product was labelled as carbon substrate.

Preparation of Zn_2NC.

Zinc acetate dihydrate (3.4 mg) and citric acid monohydrate (9.64 mg) was dissolved in 2 ml ethanol and stirred at room temperature for 1 hour to maintain the solution. Subsequently, carbon substrate (100 mg) was added to the solution, and the mixture was stirred continuously under environmental conditions for 6 hours. After drying at 80°C for 12 hours, the resulting dispersion turned into a black solid. The black solid was grinded with dicyandiamide (1 g) in a mortar and transfer the black solid into a porcelain boat. After that, the black solid was heated at 800 °C for 2 hours at a temperature rate of 5°C min^{-1} with Ar flow. The product was washed several times with 3 M HCl solution and ultrapure water, then dried at 80 °C for 12 hours to obtain Zn_2NC.

Preparation of ZnNC and NC nanosheets.

ZnNC was obtained using a similar procedure with that of Zn_2NC, with the addition of ammonia (50 μl) in the first step. For the NC nanosheets, the synthesized carbon substrate (100 mg) and dicyandiamide (1 g) were mixed thoroughly, grinded together, and heated for 2 hours using an Ar gas flow at 800°C (temperature rate of 5°C min^{-1}). Then, NC was collected through a washing process using ultrapure water and ethanol, as well as a drying process for 6 hour at a fixed temperature of 80°C.

Preparation of I_2@Zn_2NC, I_2@ZnNC, and I_2@NC composites.

I_2@Zn_2NC, I_2@ZnNC, and I_2@NC cathodes were prepared by a straightforward fusion-diffusion method. The host materials and iodine were mixed in a ratio of 1:4, then ground using a mortar for 30 minutes, and heated at 120 °C for 6 hours in a glass container under an Ar atmosphere.

The nucleation of I_2 tests

The cathode was prepared by pasting a slurry containing 80 wt% active material (I_2@Zn_2NC, I_2@ZnNC, or I_2@NC), Super P (10 wt%), and PVDF (10 wt%) onto an carbon paper collector plate. zinc metal was used as the anode, and glass fiber membrane was served as the separator. The coin cells were assembled by adding 10 μl 2 M $ZnSO_4$ solution with 0.2 M I_3^- catholyte onto the host materials and 100 μl blank electrolyte on the anode side. The cells were held at 1.25 V until the current decreased to less than 10^{-5} A.

I_3^- adsorption test

10 mg of Zn_2NC, ZnNC and NC powders were put in the 4 ml 0.02 M I_3^- solution, separately. The color change of the I_3^- solution reflects the polyiodides adsorption capacity of the host materials, and the I_3^- solution without any host material was used as a blank comparison.

In situ Raman analysis

Raman characterization was conducted on a Horiba Raman instruments, with iodine composites as cathode (I_2@Zn_2NC, I_2@ZnNC, and I_2@NC), Zn plate as anode, and

glass fiber membrane as separator. The electrolyte is 2.0 M $ZnSO_4$ in an aqueous solution. A hole with 3 mm in diameter was drilled on cathodic battery shell. The Raman signals were recorded using a 532 nm laser within the range of 50-300 cm^{-1}. The Zn-I_2 coin cell was tested at a constant current rate of 1.0 C, and the area iodine loading is ~1.0 mg cm^{-2}. For the low-temprature in-situ Raman testing, a refrigerator is placed under the battery for cooling, and a thermometer is placed on the surface of the refrigerator to monitor the temperature in real time. Other methods are similar to in situ Raman spectroscopy at room temperature.

Materials Characterizations.

Morphological information was obtained by scanning electron microscopy (SEM) using a JEOL JSM-7100F scanning electron microscope at a voltage of 10 kV. Aberration-corrected high-angle annular dark field scanning transmission electron microscopy (HAADF-STEM), transmission electron microscopy (TEM), and high-resolution transmission electron microscopy (HRTEM) images were acquired using a Titan G2 60-300 with an energy-dispersive X-ray (EDX) spectrometer. X-ray diffraction (XRD) was performed using a D8 Advance X-ray diffractometer with a non-monochromated Cu Kα X-ray source (λ = 1.054056 Å) to determine the crystallographic properties of the samples. The N2 adsorption/desorption isothermal was performed by the TriStar-3020 gas adsorption analyzer at 77 K (Micromeritics Instrument Co., USA). X-ray photoelectron spectroscopy (XPS) was performed using a VG MultiLab 2000 instrument.

Electrochemistry measurement.

Coin cells (2025-type) were assembled within an argon-filled glovebox. The cathode involved applying a slurry composed of 80 wt% active material (I_2@Zn_2NC, I_2@ZnNC, and I_2@NC), Super P (10 wt%), and PVDF (10 wt%) on a carbon paper collector plate. Subsequently, the resulting mixture underwent drying at 30℃ and was then cut into circular pellets for assembling the batteries. The pellets were utilized directly as the cathode, while zinc foil and glass fiber were utilized as the anode and the separator in 2025-type coin cells. The loading masses of different cathodes are about 1 mg cm^{-2} and the loading masses of the pouch cell is about 10 mg cm^{-2}. The thickness of Zn anodes is 0.1 mm. The electrolyte was used as 2 M $ZnSO_4$ aqueous solution. Cycling tests were conducted at a low current density during the initial few cycles. The galvanostatic charge/discharge cycling was conducted using the Neware battery test system (CT-4008-5V6A-S1-F, Shenzhen, China) with a potential range of 0.6-1.8 V vs. Zn/Zn^{2+}. The cyclic voltammetry (CV) curves were performed using an electrochemical workstation (AutolabPGSTAT302N).

Calculation methods

The first-principle-based geometry optimization calculations were carried out within density-functional theory (DFT), implemented in the Vienna Ab Initio Simulation Package (VASP) code [1], using the frozen-core projector augmented-wave (PAW) method to describe the interaction between the atomic cores and the valence electron density [2]. The exchange-correlation potential was approximated within the

generalized gradient approximation (GGA) using the Perdew-Burke Ernzerhof (PBE) functional [3]. The dispersion corrected DFT-D3 schemes was employed to describe the Van der Waals (vdW) interactions [4]. Plane-wave cutoff energy was set to 450 eV. The conjugate gradient algorithm was used in ionic optimization, convergence threshold was set to 10^{-5} eV in electronic relaxation and 0.05 eV $Å^{-1}$ in Hellmann–Feynman force on each atom. The Brillouin zone in reciprocal space was sampled by a Γ-centered Monkhorst–Pack scheme with 2 × 2 × 3 for geometry optimization and electronic structure calculations [5]. The computational hydrogen electrode (CHE) model was used to calculate the change in Gibbs free energy (ΔG) [6]. In CHE model, $H^+ + e^- \rightleftharpoons 1/2\ H2(g)$ was equilibrated at 0 V vs the reversible hydrogen electrode (RHE). The Gibbs free energy of H* adsorption was calculated as follows:

$\Delta G_* = \Delta E_* + \Delta ZPE - T\Delta S$

where ΔE_* represent adsorption energy of * (which is I^-, I_2, I_3^-), T represent temperature. ΔZPE and ΔS represent the zero point energy correction and entropy change of hydrogen adsorption, which were obtained based on vibration analysis at 298.15 K.

Reference:

[1] G. Kresse, J. Furthmüller, Efficient iterative schemes for ab initio total-energy calculations using a plane-wave basis set, Phys. Rev. B 54 (1996) 11169.

[2] G. Kresse, D. Joubert, From ultrasoft pseudopotentials to the projector augmentedwave method, Phys. Rev. B 59 (1999) 1758.

[3] J.P. Perdew, K. Burke, M. Ernzerhof, Generalized gradient approximation made simple, Phys. Rev. Lett. 77 (1996) 3865–3868.

[4] S. Grimme, J. Antony, S. Ehrlich and H. Krieg, J. Chem. Phys., 2010, 132, 154104–154123.

[5] H. J. Monkhorst and J. D. Pack, Phys. Rev. B: Solid State, 1976, 13, 5188–5192.

[6] J.K. Nørskov, J. Rossmeisl, A. Logadottir, L. Lindqvist, J.R. Kitchin, T. Bligaard, H. Jonsson, Origin of the overpotential for oxygen reduction at a fuel-cell cathode, J. Phys. Chem. B 108 (2004) 17886–17892.

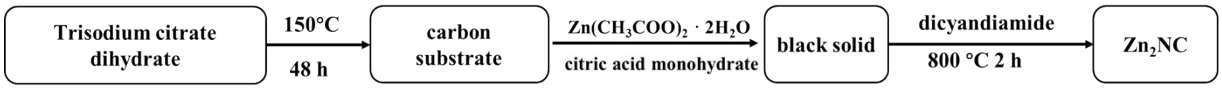

Fig. S1 A flow chart about the preparation process of Zn_2NC.

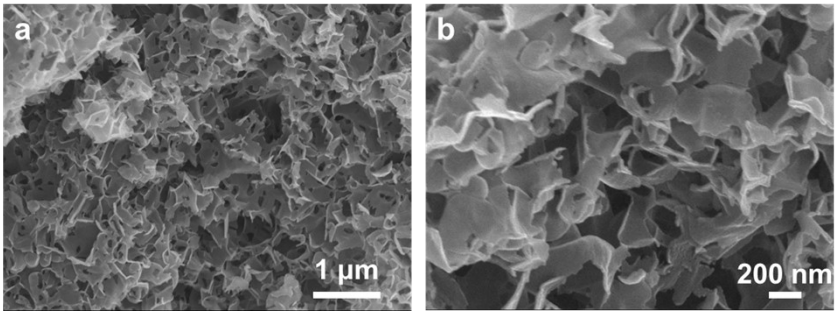

Fig. S2 The SEM images of Zn_2NC nanosheets.

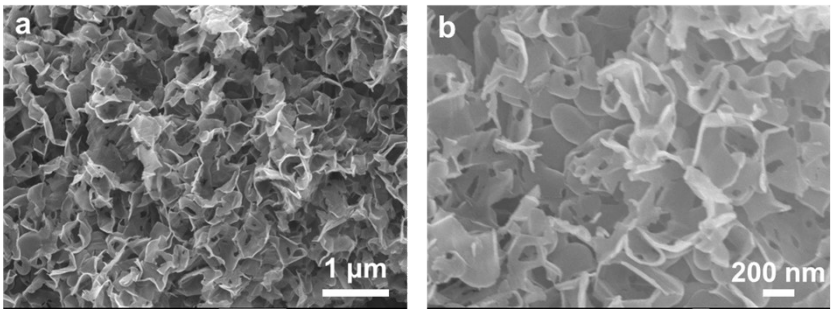

Fig. S3 The SEM images of ZnNC nanosheets.

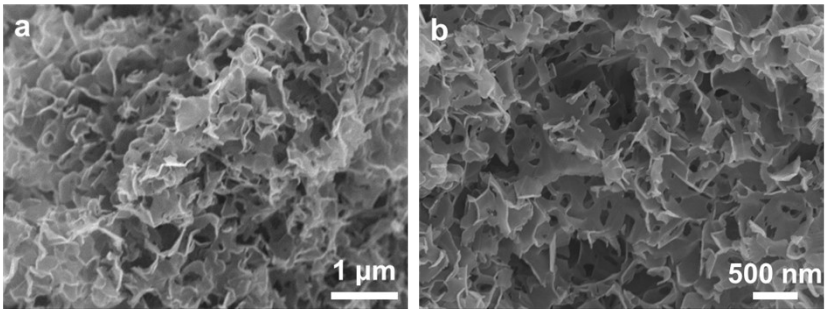

Fig. S4 The SEM images of NC nanosheets.

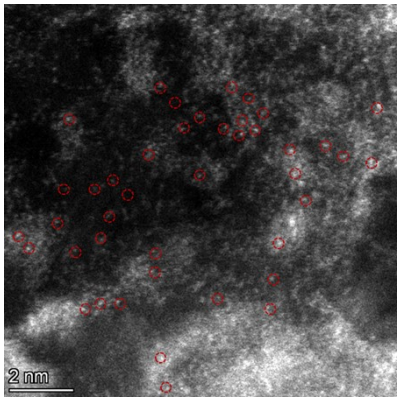

Fig. S5 Atomic-resolution HAADF-STEM image of ZnNC.

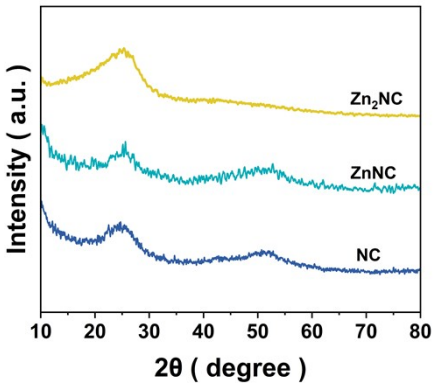

Fig. S6 XRD patterns of Zn_2NC, ZnNC and NC.

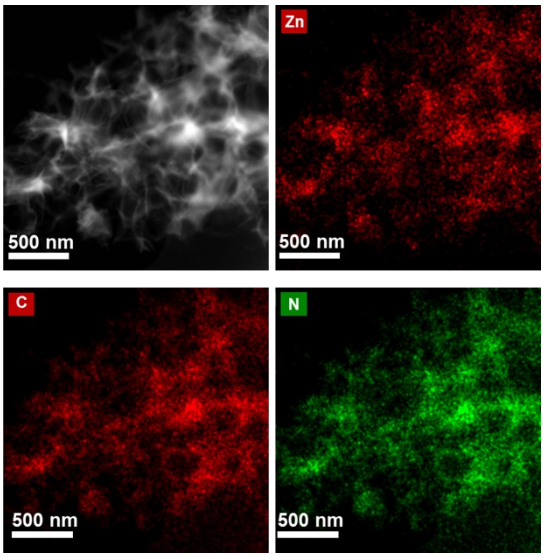

Fig. S7 The HADDF-STEM image and its corresponding EDS mappings of ZnNC.

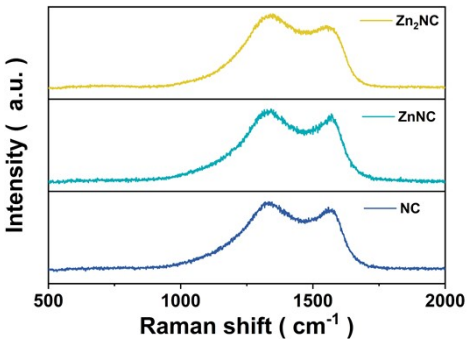

Fig. S8 Raman spectra of the Zn_2NC, ZnNC, and NC nanosheets.

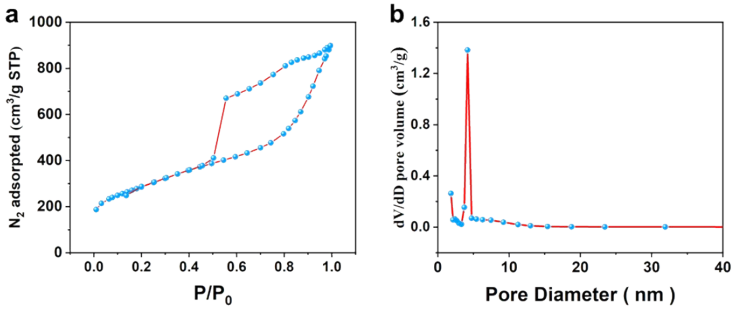

Fig. S9 N_2 adsorption-desorption isotherms of the Zn_2NC as well as its pore size distributions.

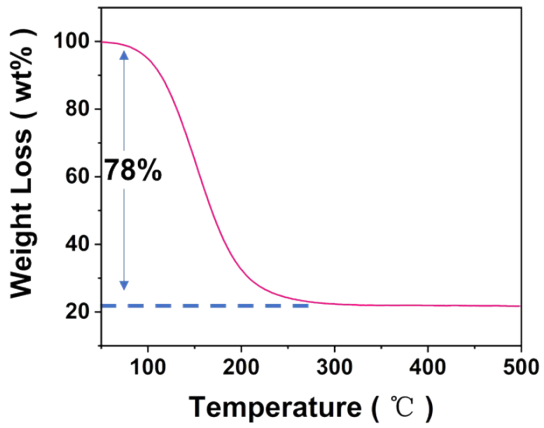

Fig. S10 TGA curve of sulfur content with normal I_2 loading.

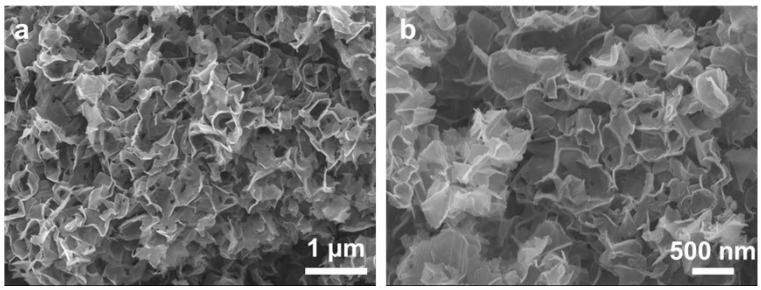

Fig. S11 The SEM images of I_2@Zn_2NC nanosheets.

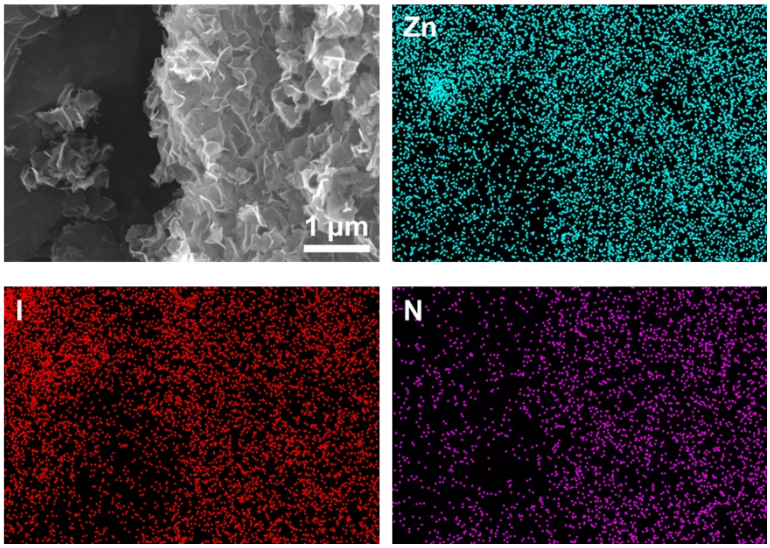

Fig. S12 The SEM images of I_2@Zn_2NC nanosheets and its corresponding EDS mappings.

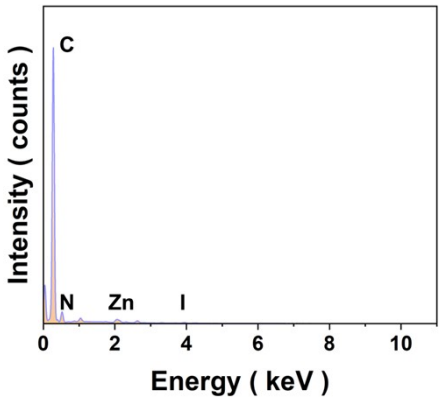

Fig. S13 The EDS mapping of I_2@Zn_2NC.

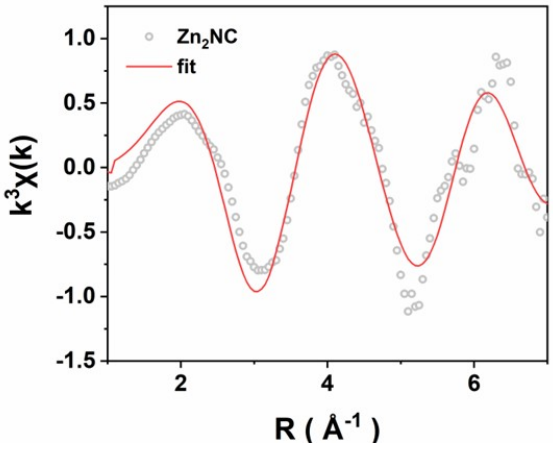

Fig. S14 K-edge k-space experimental EXAFS spectra and fitting curves of Zn.

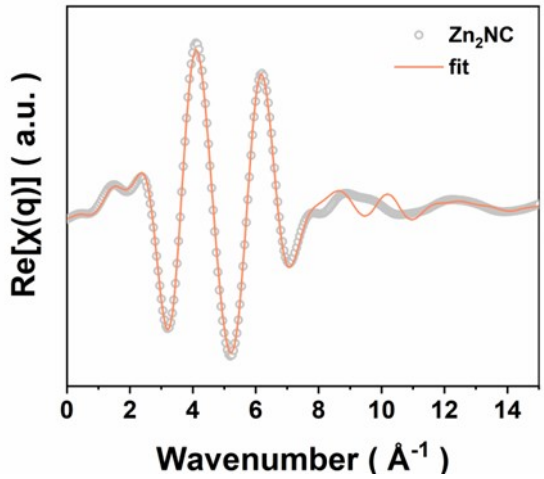

Fig. S15 XANES spectra in q space and fitting curves of Zn_2NC.

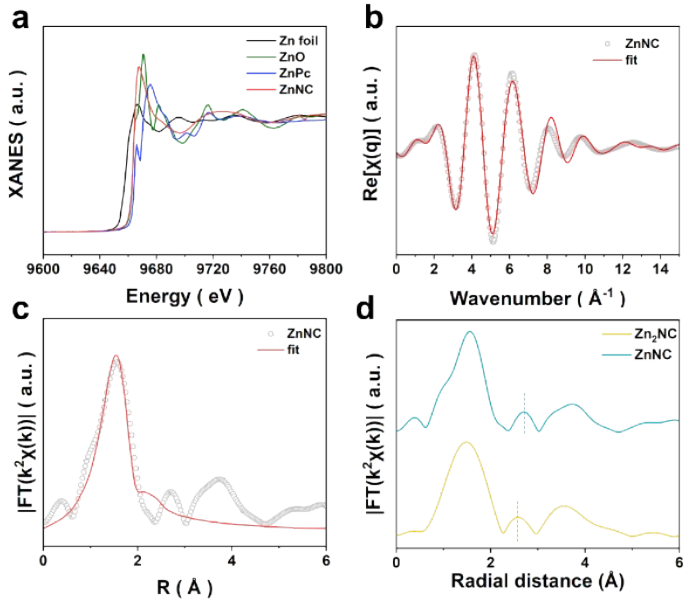

Fig. S16 (a) Zn K-edge X-ray absorption near edge structure (XANES) spectra of ZnNC, ZnO, ZnPc and Zn foil. (b) XANES spectra in q space and fitting curves of ZnNC. (c) FT-EXAFS fitting curves in the R space fitting curves of ZnNC. (d) corresponding FT results at the Zn K-edge of Zn_2NC and ZnNC.

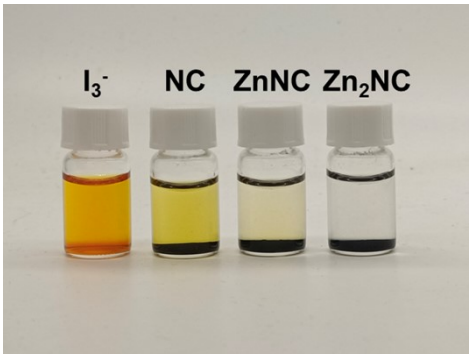

Fig. S17 Digital photo of adsorption tests of (1) bare I_3^-, (2) NC/I_3^-, (3) ZnNC/I_3^-, and (4) Zn_2NC/I_3^-, respectively.

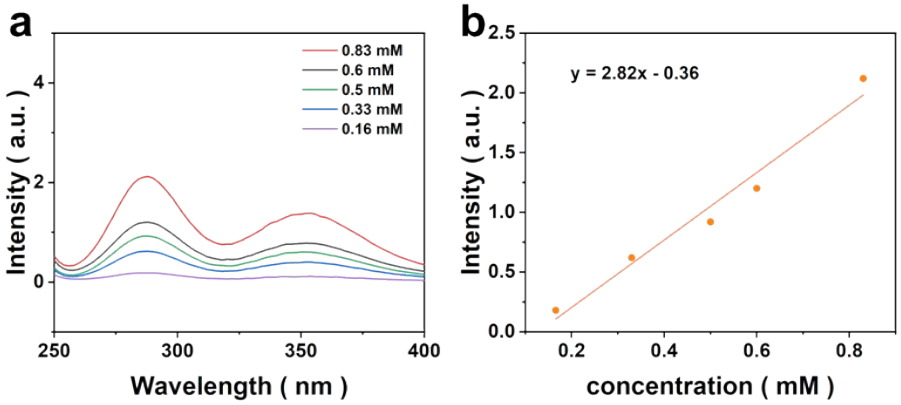

Fig. S18 UV-vis absorption spectra of different concentrations of I_3^- solutions and fitted intensity-concentration linear relationships.

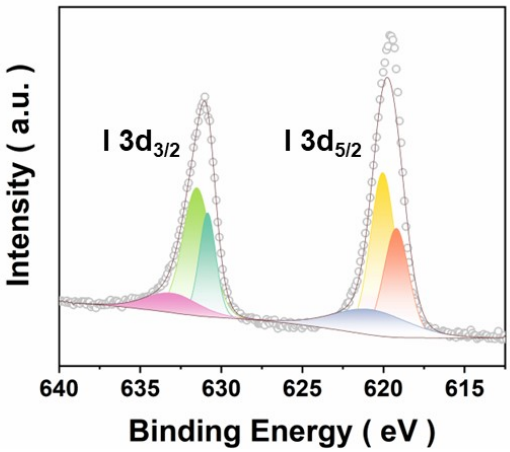

Fig. S19 XPS spectra of I 3d spectrum.

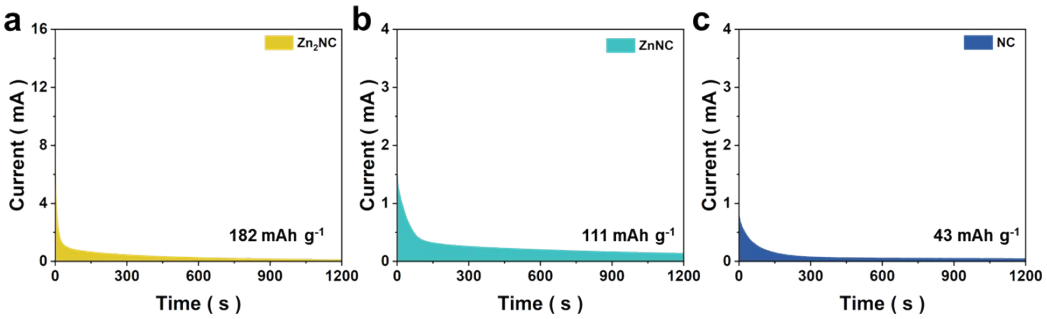

Fig. S20 The decomposition profiles of ZnI_2 with Zn_2NC, ZnNC and NC electrodes.

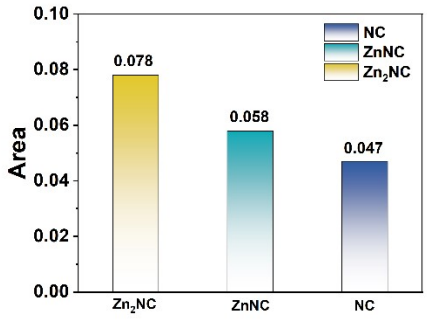

Fig. S21 Comparison of CV area for different materials.

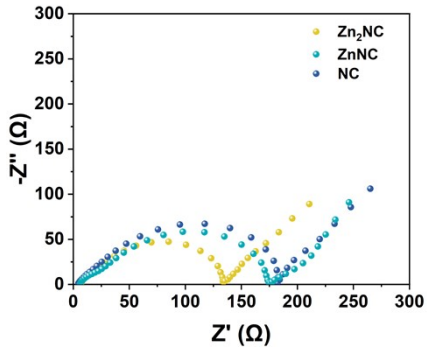

Fig. S22 The electrochemical impedance spectroscopic (EIS) spectra of Zn-I_2 battery assembled with different cathodes.

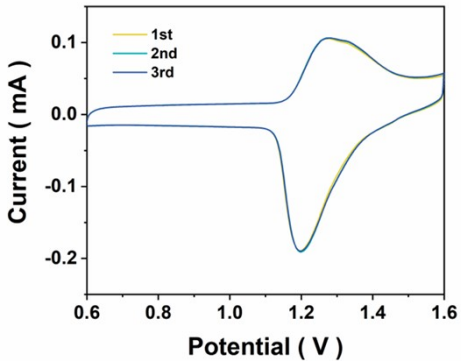

Fig. S23 The initial three CV curves of I_2@Zn_2NC cathode at 0.1 mV s^{-1}.

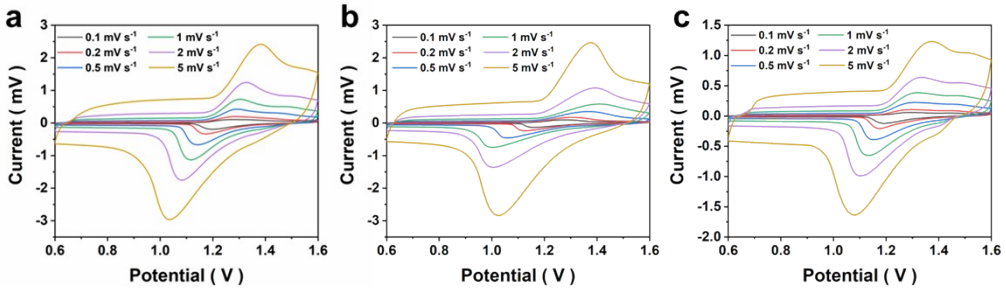

Fig. S24 CV curves of (a) I_2@Zn_2NC, (b) I_2@ZnNC and (c) I_2@NC cathodes at different scan rates in the range of 0.1-5 mV s^{-1}.

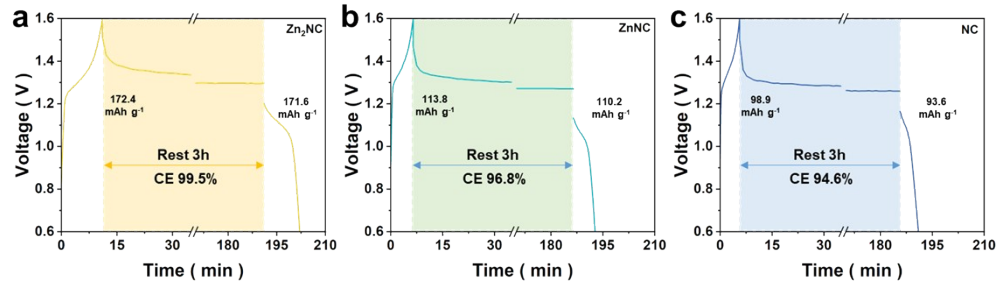

Fig. S25 Electrochemical aging test of different catalysts.

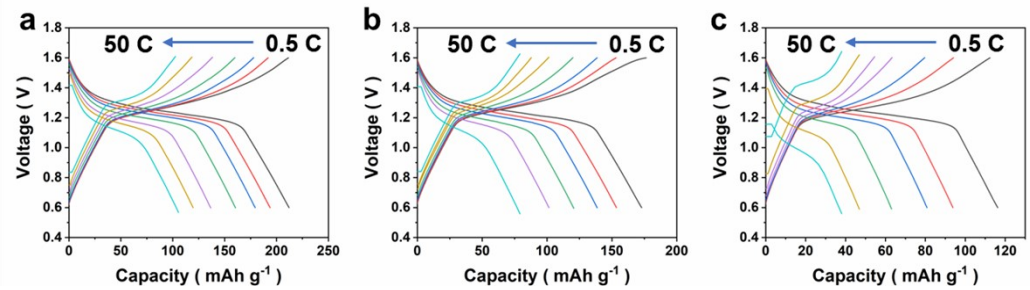

Fig. S26 Galvanostatic charge-discharge profiles of the Zn-I_2 batteries with (a) I_2@Zn_2NC cathode, (b) I_2@ZnNC cathode, and (c) I_2@NC cathode at different rates in a potential window from 0.6 to 1.6 V.

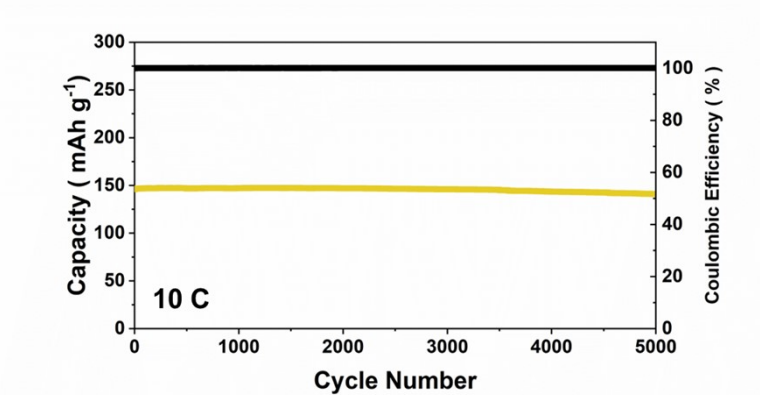

Fig. S27 Long-term cycling performance at 10 C for 5000 cycles with I_2@Zn_2NC cathodes.

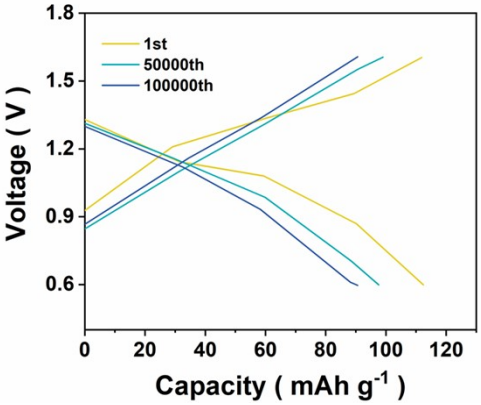

Fig. S28 Galvanostatic charge-discharge profiles of the Zn-I_2 batteries with (a) I_2@Zn_2NC cathode, (b) I_2@ZnNC cathode, and (c) I_2@NC cathode at 50 C.

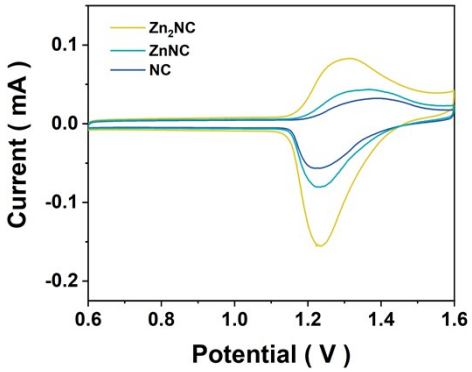

Fig. S29 CV curves at 0.1 mV s^{-1} at -20°C.

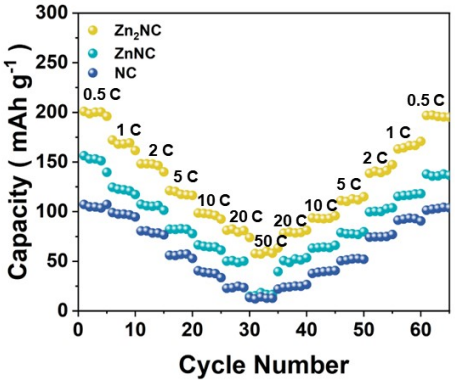

Fig. S30 Rate performances of I_2@Zn_2NC, I_2@ZnNC, and I_2@NC cathodes at -20°C.

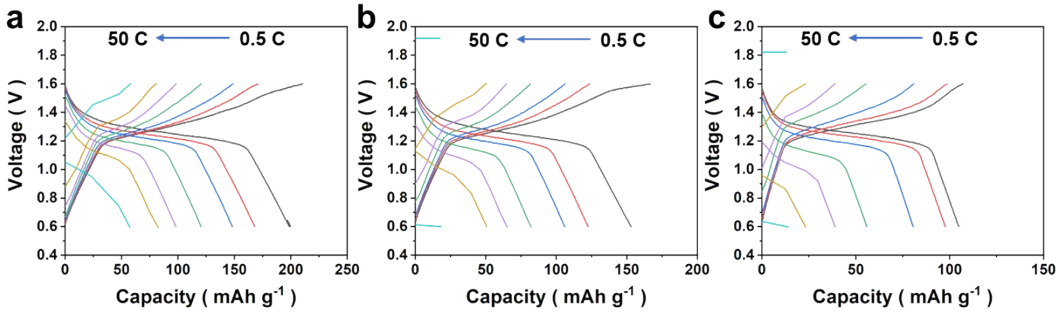

Fig. S31 Galvanostatic charge-discharge profiles of the Zn-I_2 batteries with (a) I_2@Zn_2NC cathode, (b) I_2@ZnNC cathode, and (c) I_2@NC cathode at different rates in a potential window from 0.6 to 1.6 V at -20℃.

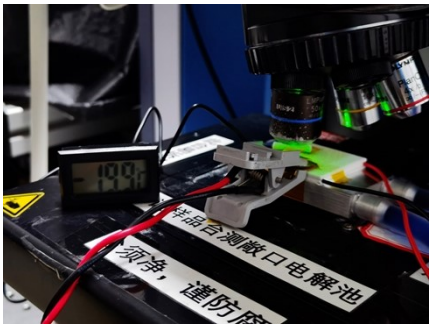

Fig. S32 Low temperature in-situ Raman spectroscopy test condition diagram.

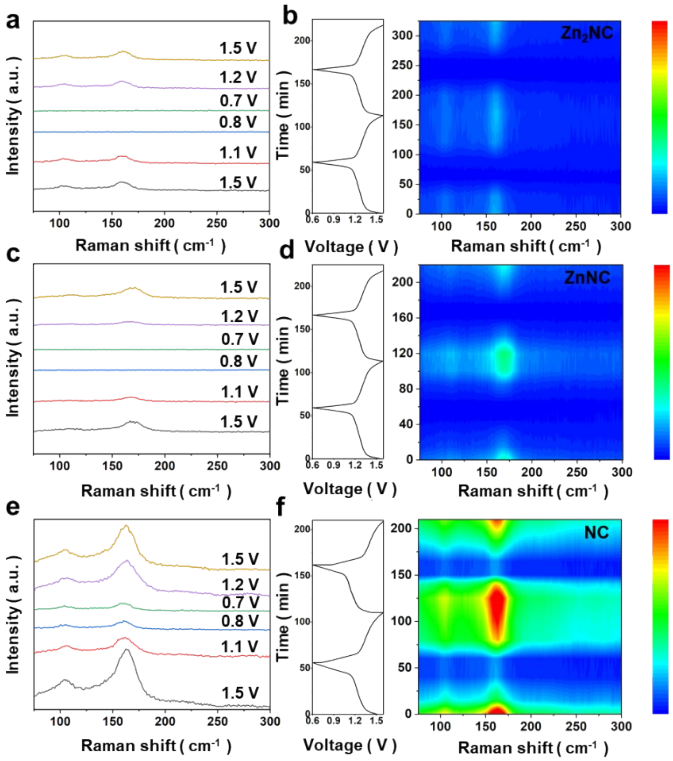

Fig. S33 Low temperature in-situ Raman spectroscopy of I_2@Zn_2NC, I_2@ZnNC and I_2@NC.

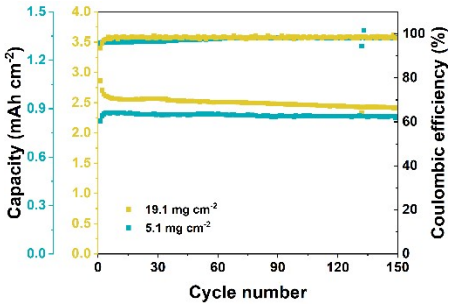

Fig. S34 Cycling performances of I_2@Zn_2NC cathodes with various iodine loadings at 1 C.

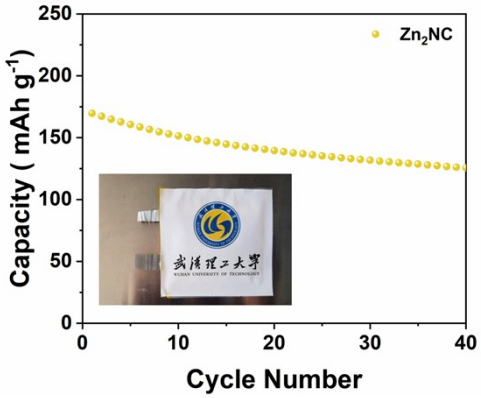

Fig. S35 Cycle performance of a pouch battery with I_2@Zn_2NC at 0.2 C. Inset: Photos of pouch Zn-I_2 battery.

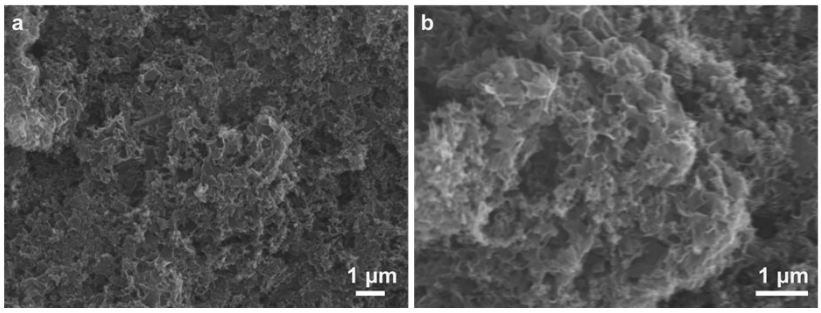

Fig. S36 The SEM images of I_2@Zn_2NC after 20 cycles.

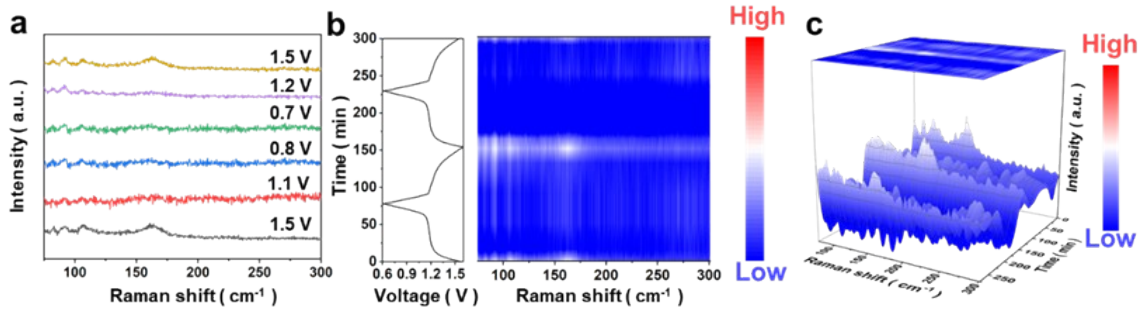

Fig. S37 In situ Raman spectrum of I_2@ZnNC. The corresponding planar and 2D and 3D in-situ time-resolved Raman spectra.

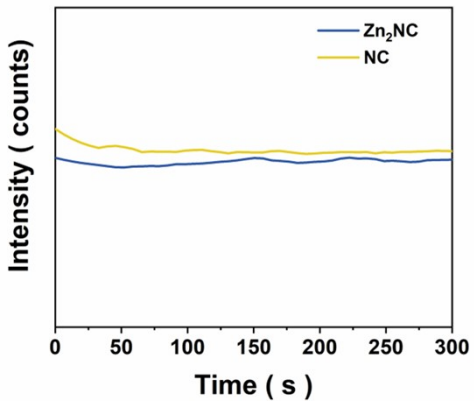

Fig. S38 ToF-SIMS 3D rendering I^- depth profile image.

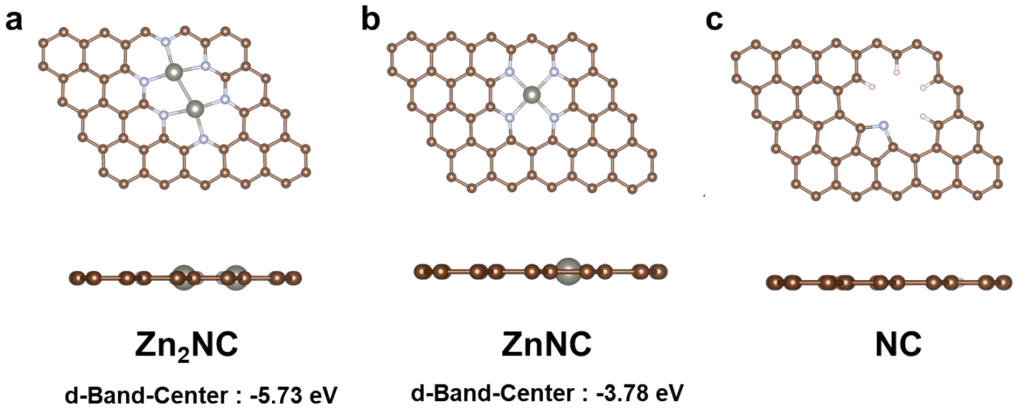

Fig. S39 The optimized configurations of (a) Zn_2NC, (b) ZnNC, (c) NC.

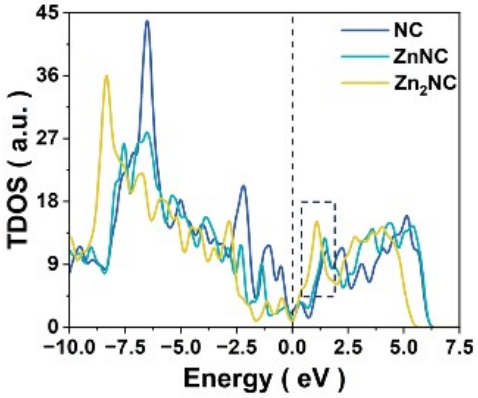

Fig. S40 The total density of states analysis of Zn_2NC, ZnNC and NC.

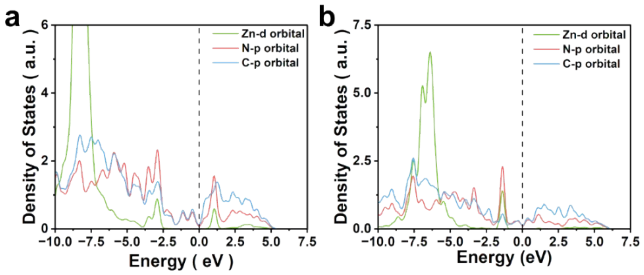

Fig. S41 PDOS of Zn-d orbitals, N-p and C-p orbitals for a) Zn_2NC and b) ZnNC.

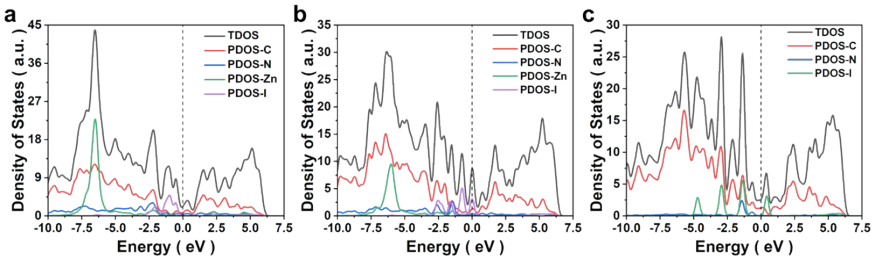

Fig. S42 Density of states analysis of (a) Zn_2NC, (b) ZnNC, (c) NC.

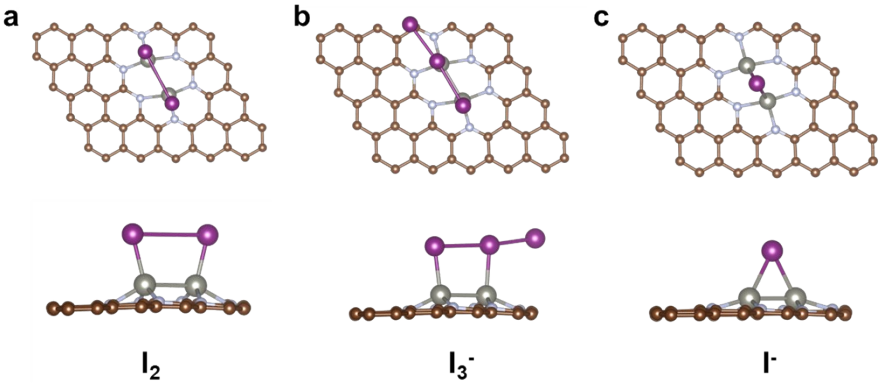

Fig. S43 Optimized configurations of polyiodides on Zn_2NC.

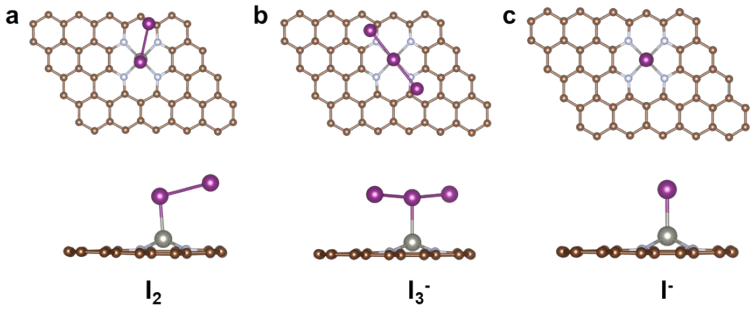

Fig. S44 Optimized configurations of polyiodides on ZnNC.

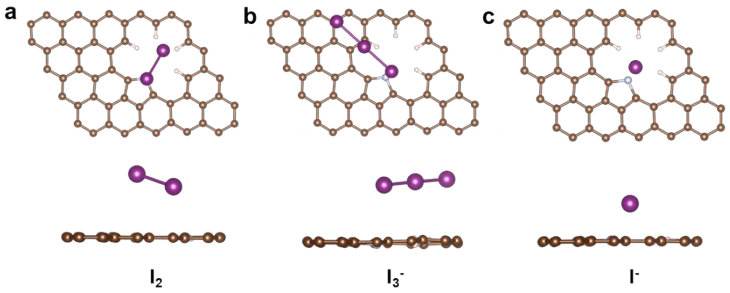

Fig. S45 Optimized configurations of polyiodides on NC.

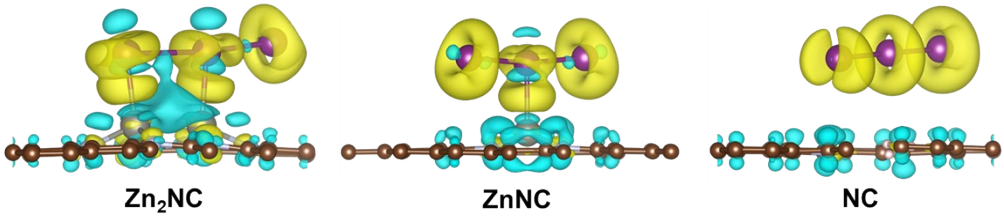

Fig. S43 Simulated deformation charge density of I_3^- on Zn_2NC, ZnNC, and NC.

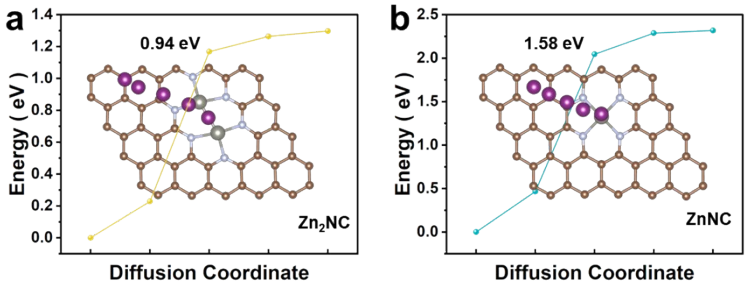

Fig. S44 Decomposition energy barriers and corresponding decomposition pathways of I_3^- on Zn_2NC and ZnNC.

Table S1 The element weight content of Zn, N, C and I in I_2@Zn_2NC was measured by EDS mapping analysis.

Weight ratio/Wt%	Zn	N	I	C
I_2@Zn_2NC	1.27	0.88	2.78	95.07

Table S2 Structural parameters extracted from the Zn K-edge EXAFS fitting.

Sample	Scattering Pair	CN	R (Å)	σ^2(Å^2)	ΔE0	R factor
Zn_2NC	Zn-N	3.1±0.3	2.00±0.05	0.0103±0.0033	4.4±1.3	0.006
	Zn-Zn	1.0±0.2	2.56±0.01	0.0106±0.0024		
ZnNC	Zn-N	4.0±0.2	2.01±0.02	0.0126±0.0031	5.2±1.4	0.019

Table S3 Comparison of the electrochemical performances of various catalysts reported in Zn-I_2 batteries.

Cathode materials	I_2 weight content (%)	Rate capacity (mAh g^{-1})	Cycle performance		Ref.
			Cycle number	Fading rate(%)	
Zn_2NC	78	114 (50 C)	100000 (50 C)	0.0002%	This work
B-Fe-NC	41.7	158 (20 C)	10000 (10 C)	N/A	[1]
$LiVS_2$	60.7	117 (25 C)	30000 (25 C)	0.0005%	[2]
Starch	N/A	75 (50 C)	50000 (50 C)	0.0002%	[3]
PNC	58	175 (20 C)	10000 (5 C)	0.005%	[4]
NCNS	50	684 (4 C)	1500 (5 C)	N/A	[5]
OSTC	26.6	175 (15 C)	10000 (5 C)	0.0015%	[6]
PBI	N/A	100 (50 C)	3500 (50 C)	0.043%	[7]
GC-PAN	70	131 (20 C)	2000 (20 C)	0.013%	[8]

Reference

[1] Liu, M.; Chen, Q.; Cao, X.; Tan, D.; Ma, J.; Zhang, J. Physicochemical Confinement Effect Enables High-Performing Zinc-Iodine Batteries. *J. Am. Chem. Soc.,* **2022**, 144, 21683-21691.

[2] Du, Y.; Kang, R.; Jin, H.; Zhou, W.; Zhang, W.; Wang, H.; Qin, J.; Wan, J.; Chen, G.; Zhang, J. Lithiation Enhances Electrocatalytic Iodine Conversion and

Polyiodide Confinement in Iodine Host for Zinc–Iodine Batteries. *Adv. Funct. Mater*., **2023**, 2304811.

[3] Zhang, S.; Hao, J.; Li, H.; Zhang, P.; Yin, Z.; Li, Y.; Zhang, B.; Lin, Z.; Qiao, S. Polyiodide Confinement by Starch Enables Shuttle-Free Zn–Iodine Batteries. *Adv. Mater*., **2022**, 34, 2201716.

[4] Liu, T.; Wang, H.; Lei, C.; Mao, Y.; Wang, H.; He, X.; Liang, X. Recognition of the catalytic activities of graphitic N for zinc-iodine batteries. *Energy Storage Mater*., **2022**, 53, 544-551.

[5] Chai, L.; Wang, X.; Hu, Y.; Li, X.; Huang, S.; Pan, J.; Qian, J.; Sun, X. In-MOF-Derived Hierarchically Hollow Carbon Nanostraws for Advanced Zinc-Iodine Batteries. *Adv. Sci*., **2022**, 9, 2105063.

[6] Chen, M.; Zhu, W.; Guo, H.; Tian, Z.; Zhang, L.; Wang, J.; Liu, T.; Lai, F.; Huang, J. Tightly confined iodine in surface-oxidized carbon matrix toward dual-mechanism zinc-iodine batteries. *Energy Storage Mater*., **2023**, 59, 102760.

[7] Gao, W.; Cheng, S.; Zhang, Y.; Xie, E.; Fu, J. Efficient Charge Storage in Zinc-Iodine Batteries based on Pre-Embedded Iodine-Ions with Reduced Electrochemical Reaction Barrier and Suppression of Polyiodide Self-Shuttle Effect. *Adv. Funct. Mater*., **2023**, 33, 2211979.

[8] Zhang, L.; Zhang, M.; Guo, H.; Tian, Z.; Ge, L.; He, G.; Huang, J.; Wang, J.; Liu, T.; Parkin, I. P.; Lai, F. A Universal Polyiodide Regulation Using Quaternization Engineering toward High Value-Added and Ultra-Stable Zinc-Iodine Batteries. *Adv. Sci*., **2022**, 9, 2105598.